

Abstract

Acknowledgements

Contents

Chapter 1

Introduction

Chapter 2

Theory

2.1 Spin-orbit coupling

2.2 Wannier Functions

In a lot of the work presented in this Thesis we construct models to describe the physics that result in a certain effect in real materials. These models are most of the time defined in terms of a limited set of local atomic-like orbitals, since these offer the most intuitive understanding most of the time, and the biggest contribution to particular effects can often be traced back to only a limited subset of all the orbitals.

If we want to apply these models to real materials to get not only qualitative, but also quantitative results, we need to perform a fit to either experimentally obtained values, or first-principles simulations. The most feasible way is usually the latter, which requires us to find a bridge between the plane waves that are used in a lot of first-principles DFT codes, and the localized basis set of that the model is built from.

Wannier functions offer a rigorous and flexible solution to this question, rewriting the Bloch functions as a discrete Fourier transform of (exponentially) localized, cell-periodic wavefunctions.

This construction is flexible in the sense that it is not unique. Bloch functions have a gauge freedom at each k value, which in turn will have an effect on the Wannier functions. One gauge that is commonly used is the one that localized the functions as much as possible, leading to the so-called Maximally Localized Wannier Functions (MLWF). Other gauges can be chosen such that the obtained functions have certain symmetries or have maximum similarity to atomic orbitals.

Chapter 3

Charge order and spin-momentum locking in high spin-orbit coupled ferroelectrics

3.1 Introduction

The research area of spintronics aims to supersede electronics by using spins instead of charges for information processing and storage. Many possible devices that utilize both charge and spin degrees of freedom of carriers have been theorized. Examples are the spin field-effect transistors (spin-FET)[1], storage devices which utilize spin-current and associated spin-transfer torque to efficiently manipulate magnetic domains [6, 5]. In spite of fundamental interest and potential for applications, the actual realization of these devices has been rather elusive. One of the main culprits for the limited success to date is that the devices require very granular, ideally electric, control of the spin, which is impeded by widely separated energy scales and weak coupling between magnetic and structural degrees of freedom. One class of materials that allow for such electric control of spin-polarized states are the ferroelectric semiconductors with large atomic spin-orbit coupling (SOC) [2, 4, 7]. The underlying mechanism is a coupling between the spin-polarized states and the ferroelectric polarization of the material that makes it possible to switch the ferroelectric polarization and in turn the polarization of the spin by the external electric field. The effect has been confirmed both experimentally [4, 9, 8], and through ab initio density functional theory (DFT) simulations [2].

3.2 Rashba-Bychkov Effect

The first effect that springs to mind bearing the signatures of the above description is the Rashba effect, first theorised in the seminal 1959 paper by Rashba and Bychkov [14]. This effect is a text book case where the breaking of a sym-

metry, in this case inversion symmetry, leads to previously degenerate states becoming nondegenerate with a definite value of the parameter describing the symmetry. In the case of the Rashba-effect, the absence of inversion symmetry leads to a breaking of the up-down symmetry of the spin of bloch functions, leading to states with definite spin polarization. These could then in turn theoretically be used in spintronics applications. We will first describe how the effect was first derived and then discuss the issues with explaining the observed spin-splitting of bloch wavefunctions in bulk ferroelectrics, and give a hint why the largest spin-polarizing effect might actually be coming from a completely different origin.

The standard derivation starts from an expansion of the electron part of the fully relativistic Dirac-equation up to second order in $1/c$ where c is the speed of light [14], in the absense of an external magnetic field:

$$\mathcal{H}\psi = \left[\frac{\mathbf{p}^2}{2m} - eV - \frac{e\hbar}{4m^2c^2}(\boldsymbol{\sigma} \cdot [\nabla V \times \mathbf{p}]) - \frac{\hbar^2}{8m^2c^2}\Delta V - \frac{\mathbf{p}^4}{8m^3c^2} \right] \psi = E\psi \quad (3.1)$$

where ψ is a two component spinor, V denotes the electric potential, $\boldsymbol{\sigma}$ a vector of Pauli-matrices ($\sigma_x, \sigma_y, \sigma_z$), m and e the electron mass and charge respectively, and \mathbf{p} the canonical momentum. The first two terms are the non-relativistic part of the Hamiltonian, the third represents the spin-orbit coupling (SOC), the fourth is known as the Darwin effect and the fifth is the relativistic correction to the effective electron mass. For the further discussion, we focus on the first three terms.

The next step is to apply the Hamiltonian to Bloch spinor wavefunctions $\psi_n(\mathbf{k}, \mathbf{r}) = u_n(\mathbf{k}, \mathbf{r})e^{i\mathbf{k} \cdot \mathbf{r}}$, where u_n denotes the cell-periodic part, and n is the band index. This leads to an eigenvalue equation for $u_n(\mathbf{k}, \mathbf{r})$

$$E_n u_n(\mathbf{k}, \mathbf{r}) = (V_0 + V_1 + V_2 + V_3) u_n(\mathbf{k}, \mathbf{r}) \quad (3.2)$$

$$V_0 = \frac{\mathbf{p}^2}{2m} - eV + \frac{\hbar^2 k^2}{2m} \quad (3.3)$$

$$V_1 = \hbar \frac{\mathbf{k} \cdot \mathbf{p}}{m} \quad (3.4)$$

$$V_2 = - \frac{e\hbar^2}{4m^2c^2} \boldsymbol{\sigma} \cdot (\nabla V \times \mathbf{k}) \quad (3.5)$$

$$V_3 = - \frac{e\hbar}{4m^2c^2} \boldsymbol{\sigma} \cdot (\nabla V \times \mathbf{p}) \quad (3.6)$$

In the following we assume that this equation can be solved for a time reversal symmetric point \mathbf{k}_0 in the first BZ, where the spin-up and spin-down part of the spinor are necessarily degenerate, and proceed following standard $\mathbf{k} \cdot \mathbf{p}$ theory to perform an expansion around this k-point. Since including the relativistic terms and nonzero \mathbf{k} will lead to spin up-down symmetry breaking, we will denote the down spin state as $|u_n^\downarrow\rangle$ and up spin state as $|u_n^\uparrow\rangle$ at $\mathbf{k} = \mathbf{k}_0$. We only investigate terms in the expansion that are linear in \mathbf{k} , since that's the part of the energy dispersion that we are seeking to explain. We again keep terms up to second order in $(1/c)^{-1}$. Without loss of generality we can take $\mathbf{k}_0 = 0$ and $E_0 = 0$.

$$E_n^{\sigma_1}(\mathbf{k}) = -\langle u_n^{\sigma_1} | V_2 | u_n^{\sigma_1} \rangle + \quad (3.7)$$

$$\sum_{m,\sigma_2=\uparrow,\downarrow} \frac{\langle u_n^{\sigma_1} | V_1 | u_m^{\sigma_2} \rangle \langle u_m^{\sigma_2} | V_3 | u_n^{\sigma_1} \rangle + h.c.}{E_n^{\sigma_1} - E_m^{\sigma_2}}, \quad (3.8)$$

where the sum over m, σ_2 includes all states which are not equal to n, σ_1 .

These two terms are of similar order of magnitude in small parameters c^{-2} and \mathbf{k} , but have different behavior with respect to the symmetries of the states, and different origins with respect to the ferroelectricity. The first term can be seen as a direct result of the electric field resulting from the ferroelectricity, i.e. ∇V there should be understood as the uniform internal electric field, whereas in the second term the ∇V should be understood as the potential which causes atomic spin-orbit coupling. This means that it is important that the orbitals u_n , and u_m in the second term originate from an atom with strong spin-orbit coupling. The reason why this term only leads to a non-zero contribution when inversion is broken can be understood by looking at the required symmetries of orbitals u_n, u_m , as was shown by [Blugel paper]. Since \mathbf{p} is odd in spatial coordinates, $\mathbf{k} \cdot \mathbf{p}$ is only non-zero when one of the orbitals is odd with respect to a spatial direction and the other even. One example could be a p_y orbital and a $s-p_z$ hybridized one, which would be created by the ferroelectricity with electric polarization along the z -axis (add drawing? add hopping matrix?).

With regards to the size of the effect, the first term usually results in a tiny splitting, due to the tiny prefactor (10^{-6}) and small \mathbf{k} value. The second term can be larger, because atomic SOC can be large for heavier atoms. There is, however, another possible source of spin splitting, originating from the so-called orbital Rashba effect (ORE).

3.3 Orbital Rashba Effect

Contrary to the relativistic effect, this one originates from electrostatic considerations. Namely, it can be shown that Bloch functions with nonzero orbital angular momentum have nonzero dipoles. This leads to two separate effects, firstly, when spin orbit coupling is included, OAM is unquenched at the high symmetry k-points, and as will be shown below, this leads to a correction to the band dispersion that varies linearly with \mathbf{k} . Secondly, this causes a linear variation of the OAM of the Bloch functions as one moves away from the high-symmetry point. If one then includes $\mathbf{l} \cdot \boldsymbol{\sigma}$ this linear \mathbf{l} will lead to an energy contribution with either positive or negative slope. To understand this contribution, we first need to understand the behavior of the orbital angular momentum of the Bloch functions in reciprocal space. This has been first described by Park et al [12], and we will give a short derivation here.

The crux is that Bloch functions with periodic part $u_n(\mathbf{k}, \mathbf{r})$ that have non-zero orbital angular momentum (OAM) create inter unit cell dipoles, which couple to the uniform electric field caused by the polarization. This will thus lead to the creation of orbitals with OAM away from high symmetry points, if symmetries allow for it and ferroelectricity is present. This effect is purely electrostatic and thus doesn't come with small prefactors like the first term in ??.

3.3.1 Tight-Binding model

Due to the breaking of inversion symmetry there are extra allowed hopping terms between unit cells, on top of the usual ones from overlap integrals. These terms originate from the energy $H_{isb} = e(\mathbf{d} \cdot \mathbf{E})$, i.e. electric dipole moments coupling to the electric field. In the following we study a toy 2D square layer with one atom per unit cell and s, p orbitals, where the field is chosen perpendicular to the 2D layer along the z direction. Assuming Wannier functions $p_\alpha(\mathbf{r}, \mathbf{R}) = \alpha e^{\left(\frac{-|\mathbf{r}-\mathbf{R}|}{a_0}\right)^2}$, we can write down the dipole matrix terms between the central unit cell and one shifted by $\mathbf{R} = \mathbf{n}a, \mathbf{n} = (n_x, n_y)$, using the basis s, p_x, p_y, p_z as follows:

$$\hat{d}_z(\mathbf{n}) = ae^{-\frac{1}{2}\left(\frac{a|\mathbf{n}|}{a_0}\right)^2} \frac{\pi^{\frac{3}{2}}}{16\sqrt{2}} \begin{pmatrix} 0 & 0 & 0 & 2 \\ 0 & 0 & 0 & n_x \\ 0 & 0 & 0 & n_y \\ 2 & n_x & n_y & 0 \end{pmatrix} \quad (3.9)$$

$$= d_z^0(\mathbf{n}) \hat{d}_z^1(\mathbf{n}). \quad (3.10)$$

Using these Wannier functions we can write down the dipoles of Bloch functions as,

$$\hat{d}_z(\mathbf{k}) = \sum_{\mathbf{n}} e^{i\mathbf{k} \cdot \mathbf{n}} \hat{d}_z(\mathbf{n}) \quad (3.11)$$

$$= \sum_{\mathbf{n}} i \sin(\mathbf{k} \cdot \mathbf{n}) \hat{d}_z(\mathbf{n}) \quad (3.12)$$

writing \mathbf{k} in terms of crystalline coordinates, and we kept only the $\sin(\mathbf{k} \cdot \mathbf{n})$ part of the exponent since the $\cos(\mathbf{k} \cdot \mathbf{n})$ part is 0 due to the fact that it is even in the sum over $\mathbf{n} = \{-\infty, \infty\}$, whereas $\hat{d}_z(\mathbf{n})$ is odd [this is not fully true, the cos term actually does contribute for the d_z^0 term, but that leads to a higher order term, should I discuss this?]. If we then assume that at $k = 0$ the Bloch functions are formed purely from these p_x, p_y, p_z Wannier functions: $|\alpha(\mathbf{k} = \mathbf{0})\rangle = \sum_{\mathbf{n}} |\alpha(\mathbf{n})\rangle$, we can write down a perturbation theory for small \mathbf{k} in the spirit of the usual $\mathbf{k} \cdot \mathbf{p}$ theory,

$$|\alpha(\mathbf{k})\rangle = |\alpha\rangle + \sum_{\beta \neq \alpha} \frac{\langle \beta | H_0(\mathbf{k}) + H_{isb}(\mathbf{k}) | \alpha \rangle}{E_\alpha - E_\beta} |\beta\rangle \quad (3.13)$$

$$= |\alpha\rangle + \sum_{\beta \neq \alpha} \frac{\langle \beta | H_0(\mathbf{k}) + eE_z \hat{d}_z(\mathbf{k}) | \alpha \rangle}{E_\alpha - E_\beta} |\beta\rangle. \quad (3.14)$$

The effect of H_{isb} is to mix p_x, p_y orbitals with the p_z orbital, e.g. if $|\alpha\rangle = |p_x\rangle$ we get that

$$|\alpha(\mathbf{k})\rangle = |p_x\rangle + i \frac{eE_z \sum_{\mathbf{n}} \sin(k_x n_x) n_x d_z^0(\mathbf{n})}{E_{p_x} - E_{p_z}} |p_z\rangle \quad (3.15)$$

$$= |p_x\rangle + i c(k_x) |p_z\rangle. \quad (3.16)$$

With $l_y = -i\hbar(z\partial_x - x\partial_z)$ we get that

$$\langle \alpha(\mathbf{k}) | l_y | \alpha(\mathbf{k}) \rangle = c(k_x) = k_x \frac{eE_z \sum_{\mathbf{n}} n_x^2 d_z^0(\mathbf{n})}{E_{p_x} - E_{p_z}} \quad (3.17)$$

[normalization!!] A similar term exists for l_x , but with the opposite sign. If the atomic spin-orbit coupling, $\lambda \mathbf{l} \cdot \boldsymbol{\sigma}$, is then taken into account, we get to a contribution to the energy dispersion $\varepsilon(\mathbf{k}) \propto E_z(k_x\sigma_y - k_y\sigma_x)$ which has exactly the form of a Rashba splitting. This shows that the inversion symmetry breaking term will lead to a linear variation of the orbital angular momentum. When the orbitals originate from an atom with non-negligible atomic spin-orbit coupling, this linear variation of the OAM will lead to a contribution to the dispersion that varies linearly with \mathbf{k} , either upwards or downwards depending on the sign of σ . Except for the atomic spin-orbit coupling, which can be large, this effect is purely based around electrostatic considerations and thus does not suffer from the same minuscule prefactor as the purely relativistic Rashba effect.

This assumes that the states at the high symmetry point ($|k| = 0$) have a fully quenched OAM, however, when spin-orbit coupling is included, this is only partially true. Due to the energy contribution from H_{soc} the material can gain by creating orbitals that have $\mathbf{j} = \mathbf{l} + \boldsymbol{\sigma}$. Similar to the above derivation, we can look at a small- k expansion for orbitals that have nonzero OAM.

We can write in general that

$$\langle \alpha | \hat{l}_\gamma | \beta \rangle = i\epsilon_{\alpha\beta\gamma} c_\alpha^* c_\beta \quad (3.18)$$

when α, β, γ designate $p_{x,y,z}$. This means that there has to be at least some admixing of multiple p -orbitals to get nonzero OAM. This leads to the following expansion of the Bloch functions around the high-symmetry $|k| = 0$ point:

$$|\psi_n(\mathbf{k})\rangle = \sum_{\mathbf{n}, \alpha} c_\alpha(\mathbf{k}) e^{i\mathbf{k} \cdot \mathbf{n}} |\alpha(\mathbf{n})\rangle \quad (3.19)$$

$$= \sum_{\mathbf{n}, \alpha} \left(c_\alpha(0) + \mathbf{k} \frac{\partial c_\alpha(\mathbf{k})}{\partial k} \Big|_{\mathbf{k}=0} \right) (1 + i\mathbf{k} \cdot \mathbf{n}) |\alpha(\mathbf{n})\rangle. \quad (3.20)$$

If we then calculate the linear-with- k varying dipole moment of these Bloch functions, we can recognize the contribution coming from the second term in the c expansion together with the first term in the e expansion as the previously discussed contribution. We can, however, also combine the first term in the c expansion with the second in the e expansion. If we single out this contribution to $d_z(\mathbf{k})$ we get

$$d_z(\mathbf{k}) = i \sum_{\mathbf{n}, \alpha, \beta} c_\alpha^*(0) c_\beta(0) \mathbf{k} \cdot \mathbf{n} \langle \alpha(\mathbf{0}) | \hat{d}_z | \beta(\mathbf{n}) \rangle \quad (3.21)$$

$$= i \sum_{\mathbf{n}} d_z^0(\mathbf{n}) (c_x^*(0) c_z(0) k_x n_x^2 + c_y^*(0) c_z(0) k_y n_y^2) \quad (3.22)$$

$$= \sum_{\mathbf{n}} d_z^0(\mathbf{n}) (l_x(0) k_y n_y^2 - l_y(0) k_x n_x^2). \quad (3.23)$$

[normalization!!] These expressions show us that, together with $H_{soc} = \lambda \mathbf{l} \cdot \boldsymbol{\sigma}$ and $H_{isb} = eE_z d_z$, an additional Rashba-like term will appear in the energy dispersion [maybe a little more explanation is warranted here].

With the understanding that one can find Rashba like dispersions, coming not from the usually considered purely relativistic, but also from electrostatic means, we can look at an example situation where this leads to a gigantic spin-splitting in a bulk material, namely Germanium Telluride (GeTe).

3.4 Overview: Germanium Telluride

The space group of GeTe is $R\bar{3}m$ (#160 in International Tables), with ferroelectric polarization along the threefold rotation z -axis caused by an off-centering of the central Te atom [13] as displayed in Fig. ??-(a). The valence and conduction bands are formed mostly by s and p orbitals from Te and Ge, respectively. This, together with the large spin-splitting in the vicinity of the Z point [2] as observed from the bandstructure in Fig. ??-(b), lends it as a perfect test-case of the above described mechanisms. Moreover, since it's a bulk material, we can rule out the possibility that the relativistic Rashba effects results in a contribution from the existence of possible large potential gradients at a surface. The band structure, presents a distinct large linear spin splitting around the Z point, resembling the well known Rashba effect. Due to time reversal symmetry, no spin-splitting is only present observed along the $Z - A$ and $Z - U$ paths, not the $Z - \Gamma$ path. The density of states (DOS), displayed in Fig. ??-(c), confirms the orbital character of the bands, aluded to earlier.

3.5 Methods

To analyze and confirm the earlier made statements and observations, we performed ab-initio DFT calculations using the Quantum-Espresso software package[3]. Both non- and fully-relativistic calculations were performed to confirm the existence of the linear varying OAM even when spin-orbit is not included. Both calculations were performed using ONCVPSP pseudopotentials, with energy cutoffs of 40 Ry for the energy cutoff, and 160Ry for the density cutoff. The reciprocal space was sampled using a 10x10x10 and 6x6x6 Monkhorst-Pack grid for the self-consistent and non-self-consistent calculations, respectively, using an energy convergence threshold of 10^{-7} . Afterwards we used the Wannier90 [11] package to perform the Wannierization, using atomic s and p -orbitals on both Ge and Te. This provides us with the tools to analyse the localized properties of the Bloch functions such as the dipole moment and OAM.

3.6 Band structure

The bands we will focus on most are the three topmost valence bands. As seen in Fig. ??-(a), these bands have the largest spin-splitting, giving already a hint that as shown above, the atomic SOC is an important part, since it's bigger on Te, where the orbitals comprising these bands originate from. If one were to fit the dispersion from the topmost valence band to the form of the Rashba Hamiltonian [14, 10],

$$\mathcal{H}_R = \alpha_R(\mathbf{k} \times \mathbf{E}) \cdot \boldsymbol{\sigma}, \quad \alpha_R = \frac{e\hbar^2}{2m^2c^2}, \quad (3.24)$$

it would result in an abnormally large $\alpha_R \approx 30.7 \text{ eV}\cdot\text{\AA}$ [2], while, as discussed before, a more realistic prefactor would be $\alpha_R = 10^{-6} \text{ eV}$ in the purely relativistic case inside the vacuum. This is even more abnormal considering the fact that this is a bulk material, and that it is known that proper ferroelectrics have zero polarization in open boundary conditions because the depolarizing fields are not screened. Moreover, in the periodic boundary conditions utilized by DFT, the potential mimics short circuit boundary conditions [**Meyer2008AbFields**], $\mathbf{E} = 0$, which results in zero contribution from Eq. ??.

The last issue with the purely relativistic explanation, which has been confirmed experimentally[8], lies in the orientation of the spin polarization of the split bands. According to Eq. ??, they should all be lined up. However, as has been shown and will be confirmed by our results below, the orientation depends on the character of the band, more specifically the value of the total angular momentum j .

3.7 Results and Discussion

The dispersion, OAM, and SAM of the first valence band are shown in the left panel of Fig. ???. Confirming our earlier conclusions, we can see that non-zero, linearly varying OAM is formed as we move away from the high-symmetry Z -point. Moreover, the OAM is perpendicular to both the z -axis and the k vector, as it should be from Eq.???, and can also be seen from the panels in Fig. ???. This leads e.g. to $l_y = 0$ along the $A \rightarrow Z$ path, where only k_y is nonzero. When atomic SOC is included in the orange and blue graphs, we see the spin-splitting that results from having the spin oriented either along or opposite to the already linearly varying OAM. The unquenching of the OAM at the Z -point when SOC is included is also clearly visible, together with the resulting change in the slope that originates from the corresponding contribution to the dipole moment Eq. ???. This correlation can also be observed in the panel showing the center of mass $\bar{z} = \int_{\text{supercell}} z|\psi(k)|^2$ of the Bloch-functions, which is proportional to the dipole moment around the same reference point.

When we compare this first valence band with the third valence band, shown in the right panel of Fig. ???, we can clearly see the previously discussed issues with the purely relativistic explanation. As stated before, we can note that not only the magnitude but also the sign of α_R in ?? is opposite for these two bands, showcased by the size of the splitting, and by the ordering of the spin-up vs the spin-down splitted part. This is because the character of the first and third valence bands are different. The first valence band is mostly coming from Te $j = \frac{3}{2}$ orbitals, whereas the third valence band is predominantly $j = \frac{1}{2}$. This causes the orientation of the OAM and SAM to be along each other in the first band, and opposite for the third, as shown in Fig. ???. This then leads to the different ordering of the spin-split bands.

There is one last very interesting feature one can notice from Fig. ?? (c) and (f), that is, the switching of the character (and SAM, OAM orientation) of the bands, very close to the Z point. This is because Eq. (??) breaks threefold symmetry causes the atomic j to not be a conserved quantity, i.e. there is a mixing between different atomic j orbitals, in this very narrow region around Z .

All these considerations lead to a very nontrivial SAM and OAM texture of

the bands as we progress through the BZ.

3.8 Conclusions

We have explored the microscopic origin of the giant Rashba-like spin splitting in the band structure of bulk ferroelectric GeTe with high atomic SOC. We derived the form of the band dispersion in the Wannier representation, that relates the large spin splitting to the intricate interplay between OAM, atomic SOC, the crystal field and the electric polarization. It turns out that the crucial component, which is not present in the relativistic Rashba effect, is the emergence of a nonzero electric dipole of the Bloch functions due to their OAM. The quantitative analysis based on Wannier functions and atomic-centered approximation confirms this mechanism in GeTe. We find a very good agreement between the proposed band dispersion, Eq. (??), and the dispersions of the first and third valence bands, where the effect manifests itself most clearly.

Ultimately, the results suggest that (1) large ferroelectric polarization, (2) high atomic SOC, and (3) highly symmetric environment producing little OAM quenching could be the design rules for new materials with strong Rashba-like spin splitting. These materials could enable spintronic devices with the much needed electric control of spin polarization.

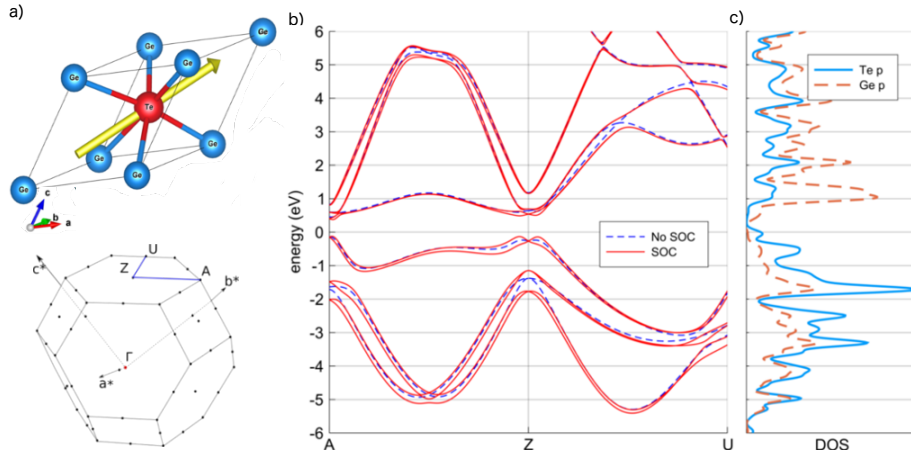


Figure 3.1: (a) Rhombohedral unit cell and Brillouin zone of GeTe, with the polarization direction in yellow. (b) Band structure obtained from a DFT calculation with and without SOC, along the blue path in panel (a). (c) partial DOS for Te and Ge p orbitals computed without SOC.

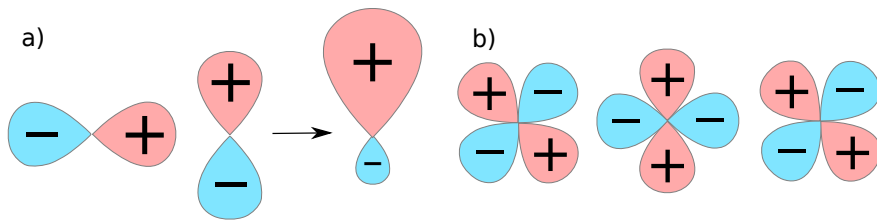


Figure 3.2: Overlap dipoles of orbitals in neighboring unit cells. (a) Nonzero dipole coming from shifted p orbitals. (b) Dipoles of shifted d orbitals compensate at a high symmetry point.

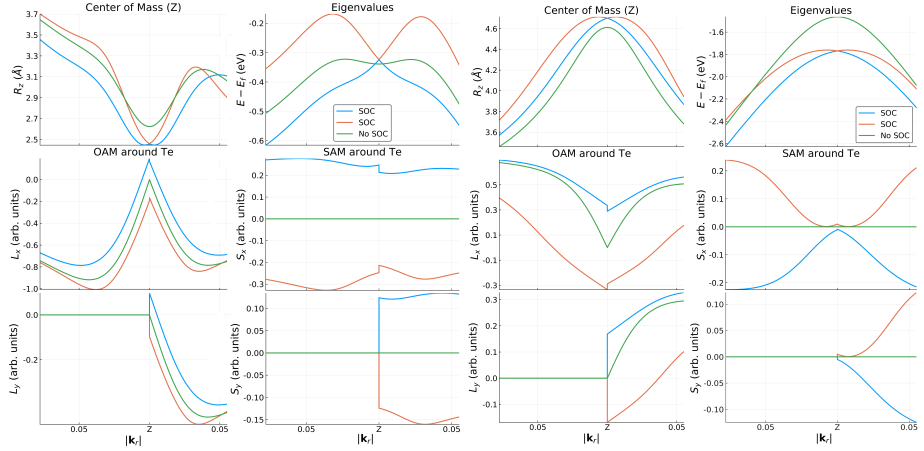


Figure 3.3: Comparison between the real-space observables and energy dispersion in (a) the first and (b) third valence band. The values are plotted in function of the relative distance from the Z point $\mathbf{k}_r = \mathbf{k} - \mathbf{k}_Z$, towards the A and U points. The green graphs denote the values before turning on atomic SOC, whereas the orange and blue graphs denote the two spin-split bands.

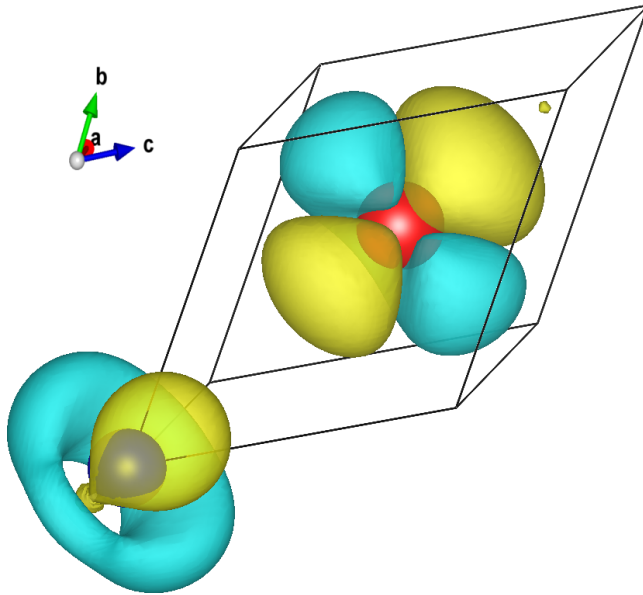


Figure 3.4: The variation of the charge density of the Bloch function of the first valence band $\frac{\partial |\psi(\mathbf{k})|^2}{\partial \mathbf{k}} \Big|_{\mathbf{k}=Z}$ away from Z towards A . Te and Ge ions are in red and blue, respectively. The charge asymmetry around Ge showcases the nonzero dipole moment along z , which couples to the local electric field near Ge ion.

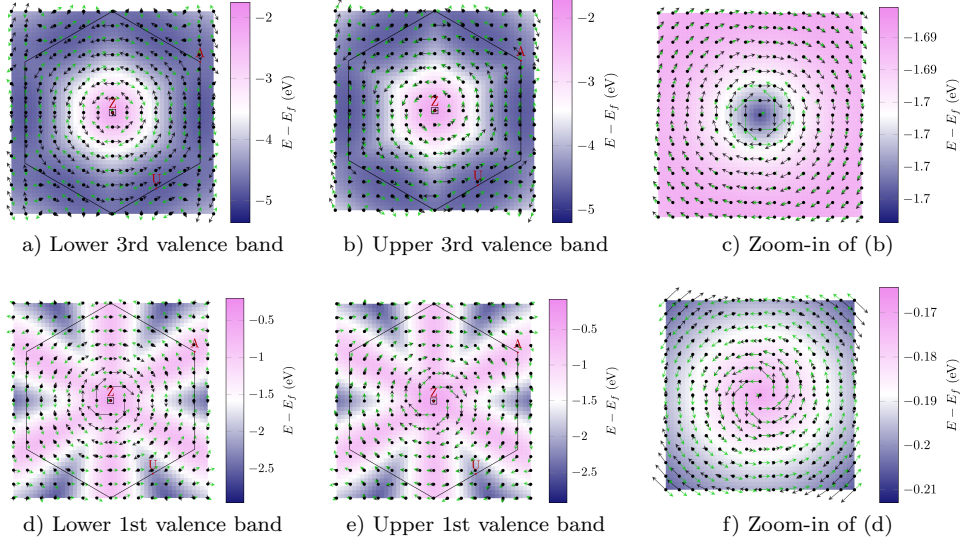


Figure 3.5: OAM and SAM textures around the Z point in the first and third valence bands of GeTe. The black and green arrows show the OAM and SAM textures, respectively. The length of the arrows was chosen separately for clarity in each figure and should thus not be compared. The color maps signify the energy of the bands, relative to the Fermi level. The small box around the Z point indicates the area, magnified in panels (c) and (f). In the zoomed figures (c) and (f) one can observe the change or relative orientation between the SAM and OAM when moving away from the Z point, signifying a change of character between $j = 1/2$ and $j = 3/2$.

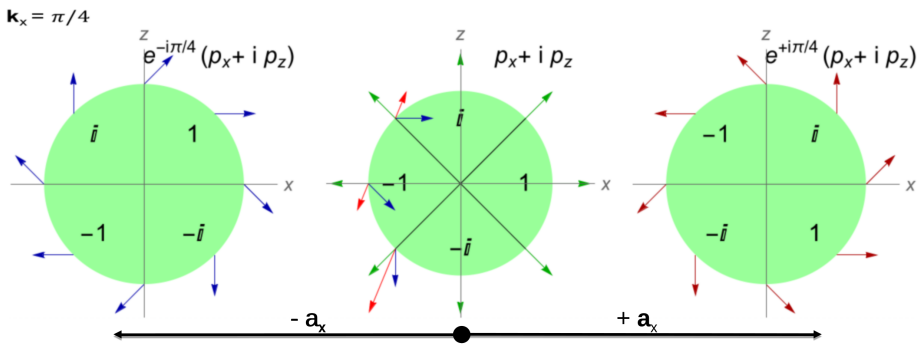


Figure 3.6: Interference between orbitals with nonzero OAM. Three neighboring unit cells are displayed, each with the same $p_x + ip_z$ orbital (thus having nonzero l_y). The wave functions of the left and right unit cells have their phase rotated by the plane-wave part $e^{ik_x R_x}$. The amplitude and phase of the wave function are encoded with the length and polar angle of the arrows.

Bibliography

- [1] Supriyo Datta and Biswajit Das. “Electronic analog of the electro-optic modulator”. In: *Applied Physics Letters* 56.7 (1990), pp. 665–667. ISSN: 00036951. DOI: 10.1063/1.102730.
- [2] Domenico Di Sante et al. “Electric control of the giant rashba effect in bulk gete”. In: *Advanced Materials* 25.4 (2013), pp. 509–513. ISSN: 09359648. DOI: 10.1002/adma.201203199.
- [3] Paolo Giannozzi et al. “QUANTUM ESPRESSO: a modular and open-source software project for quantum simulations of materials.” In: *Journal of physics. Condensed matter : an Institute of Physics journal* 21.39 (2009), p. 395502. ISSN: 0953-8984. DOI: 10.1088/0953-8984/21/39/395502.
- [4] K Ishizaka. “Giant Rashba-type spin splitting in bulk BiTeI”. In: *Nature materials* 10.7 (2011), pp. 521–526. ISSN: 1476-1122. DOI: 10.1038/nmat3051. URL: <http://dx.doi.org/10.1038/nmat3051>.
- [5] T Jungwirth et al. “Antiferromagnetic spintronics”. In: *Nature Nanotechnology* 11.3 (2016), pp. 231–241. ISSN: 1748-3387. DOI: 10.1038/nnano.2016.18. URL: <http://www.nature.com/doifinder/10.1038/nnano.2016.18>.
- [6] Andrew D. Kent and Daniel C. Worledge. “A new spin on magnetic memories”. In: *Nature Nanotechnology* 10.3 (2015), pp. 187–191. ISSN: 1748-3387. DOI: 10.1038/nnano.2015.24. URL: <http://www.nature.com/doifinder/10.1038/nnano.2015.24>.
- [7] Minsung Kim et al. “Switchable $S = 1/2$ and $J = 1/2$ Rashba bands in ferroelectric halide perovskites.” In: *Proceedings of the National Academy of Sciences of the United States of America* 111.19 (2014), pp. 6900–4. ISSN: 1091-6490. DOI: 10.1073/pnas.1405780111. URL: <http://www.pnas.org/cgi/content/long/111/19/6900>.
- [8] J. Krempaský et al. “Surface versus bulk contributions to the giant Rashba splitting in the ferroelectric $\{\alpha\}$ -GeTe(111) semiconductor”. In: 111 (2015), pp. 1–10. DOI: 10.1103/PhysRevB.94.205111. URL: <http://arxiv.org/abs/1503.05004%0Ahttp://dx.doi.org/10.1103/PhysRevB.94.205111>.
- [9] Marcus Liebmann et al. “Giant Rashba-Type Spin Splitting in Ferroelectric GeTe(111)”. In: *Advanced Materials* 28.3 (2016), pp. 560–565. ISSN: 15214095. DOI: 10.1002/adma.201503459.

- [10] E. M. Lifshitz, V. B. Berestetskii, and Lev Petrovich Pitaevskii. *Course of Theoretical Physics - Volume 4: Relativistic Quantum Theory*. 2nd Edition. Elsevier, 1982. URL: <http://ci.nii.ac.jp/ncid/BA20776995>.
- [11] Arash A. Mostofi et al. “An updated version of wannier90: A tool for obtaining maximally-localised Wannier functions”. In: *Computer Physics Communications* 185.8 (2014), pp. 2309–2310. ISSN: 00104655. DOI: 10.1016/j.cpc.2014.05.003.
- [12] Seung Ryong Park et al. “Orbital-angular-momentum based origin of rashba-type surface band splitting”. In: *Physical Review Letters* 107.15 (2011), pp. 1–5. ISSN: 00319007. DOI: 10.1103/PhysRevLett.107.156803.
- [13] K. M. Rabe and J. D. Joannopoulos. “Theory of the structural phase transition of GeTe”. In: *Physical Review B* 36.12 (1987), pp. 6631–6639. ISSN: 01631829. DOI: 10.1103/PhysRevB.36.6631.
- [14] Emmanuel Rashba and V. Sheka. “Symmetry of Energy Bands in Crystals of Wurtzite Type II . Symmetry of Bands with Spin-Orbit Interaction Included The Harvard community has made this article openly available . Please share how this access benefits you . Your story matters . Accessed (Ar” . In: *Fiz. Tverd. Tela: Collected Papers* 2 (1959), pp. 162–76.

Chapter 4

Coupling between spin and strain density waves

4.1 Introduction

The coupling between orders

4.2 Theory

[some explanation of Peierls instabilities etc, the things that cause the SDW in the first place?]

In materials where spin-density waves (SDW) are formed, there are often also secondary periodic lattice displacements leading to strain waves. This can be understood from magnetostriction, where in the usual Heisenberg form

$$H = \sum_{\langle i,j \rangle} J_{ij} \mathbf{S}_i \cdot \mathbf{S}_j, \quad (4.1)$$

derived from second order perturbation theory in t^2/U of the Hubbard model,

$$H = \sum_{\langle i,j \rangle} t_{ij} c_{i,\sigma}^\dagger c_{j,\sigma} + U \sum_i n_i^\uparrow n_i^\downarrow \quad (4.2)$$

we find that the coupling constant $J_{ij} = t_{ij}^2/U$, where $t_{i,j}$ denotes the hopping parameter between the orbital on site i to the one on site j . It is clear that this hopping parameter depends on the bond length between the two sites, leading to an increase in J_{ij} when the bond length goes down and vice versa when it increases. If then a particular magnetic configuration, as e.g. a SDW, is enforced in the material, bond lengths will be optimized to minimize the contribution to the energy from $??$. This is what causes the secondary strain wave or PLD.

In order to model this coupling between the order parameters throughout the material, we adopt a continuum Landau model with two order parameters L and y for the antiferromagnetic SDW and PLD respectively. We use a fourth order expansion in terms of both parameters leading to the Landau free energy given by

$$F = \frac{\alpha}{2} (T_L - T_c) L^2 + \frac{\beta}{4} L^4 - g L^2 y + \frac{\omega_0}{2} y^2 + \frac{b}{4} y^4. \quad (4.3)$$

The double well potential that leads to the SDW is characterised by α and β , with the temperature of the SDW is given by T_L , with the critical temperature T_c , above which the phase transition occurs and the order gets destroyed. The coupling between the two order parameters is given by term with γ , where L is to second power because energy is time-reversal even whereas L is time-reversal odd. Notice that the PLD order parameter y by itself would not have a nonzero equilibrium value, the fourth order term with b is only to provide a better fitting to some anisotropic features of the experiment that we are looking to describe. The equilibrium value of y will however be shifted away from 0 due to the force applied to it by the nonzero L , a key feature of this model to bear in mind for later. y is thus a pure slave order parameter.

In order to describe the heating of the SDW through the photoexcitation caused by the XFEL pulses, we use a two temperature model given by

$$c_L T'_L = -k(T_L - T_b) + q(t) \quad (4.4)$$

$$c_b T'_b = -k(T_b - T_L) \quad (4.5)$$

where b denotes the variables and parameters associated with a universal bath, c_L, c_b are the heat capacities of the SDW and the bath, k the heat transfer rate, and $q(t)$ signifies the heat injected into the system through the photon pulses, and is modeled by a gaussian $q(t) e^{-(t-t_0)^2/\tau^2}$, where τ denotes the pulse width. The primes signify time derivatives.

In order to solve the time evolution of the system we start by incorporating the free energy given by Eq. ?? into the full Lagrangian

$$\mathcal{L} = \frac{m_L(\dot{L} + \gamma_L L)^2}{2} + \frac{m_y(\dot{y} + \gamma_y y)^2}{2} - F, \quad (4.6)$$

where the γ denote the damping parameters for both order parameters. This then leads to the well-known Euler-Lagrange equations given by

$$m_L \ddot{L} = -\alpha(T - T_c)L - \beta L^3 + 2gL\dot{y} - \gamma_L \dot{L} \quad (4.7)$$

$$m_y \ddot{y} = gL^2 - \omega_0^2 y - b\dot{y}^3 - \gamma_y \dot{y} \quad (4.8)$$

which we then solve numerically to get the time evolution of both order parameters.

4.3 Experimental methods

Before focusing on the theoretical description of the coupling between the SDW and CDW, we take a look at the experimental techniques and results that we are seeking to reproduce. Optical pulses were used to heat up the material, mostly absorbed by the SDW order through photoexcitation. An x-ray free-electron laser (XFEL) is then used to probe the bragg-peaks of the CDW and how they change in time. The need of the XFEL can be attributed to the very short timescales at which the observed behavior is exhibited by the material, with resolutions of a couple femtoseconds being made accessible. The scattering intensity of the bragg peak is directly proportional to the magnitude of the CDW, offering both phase and amplitude information of the oscillation that we study. It is important to realize that the SDW order is not directly accessible

through these kinds of measurements, so we are effectively studying the effect of exciting one order parameter through the reaction of the other due to the coupling between them. XFELs also allow for higher peak selectivity (narrow and intense satellite Bragg peaks), such that it allows for measurements performed on thin films even deposited on thick substrates, as was the case in the experiments performed by A. Singer et.al. The thin films offer a clarity in terms of describing the physics of this process, since it leads to a very even excitation of the entire volume, and it causes the order parameters to be homogeneous throughout the material. This absence of topological defects is confirmed by the absence of a widening of the satellite peak associated with the PLD, as compared with the peaks of the material itself. [not sure about this, I actually don't understand what they are talking about in the paper either]. To this end, a 30nm thick Cr film was used in the experiments, harboring seven periods of the SDW perpendicular to the plane. This thinness of the film also decreases the Neel temperature to 290K, from the bulk value of around 307K. The pulses used to excite the SDW were 40 fs long, with a total intensity of 2.9 mJ/cm^2 . In the experiments with two sequential pulses the power of the second pulse was roughly half that of the first.

4.4 Results

The experimental results we use as a basis to fit our model to are shown in Fig. ???. In the numerical model, we found in earlier trials that the dynamics of the SDW order parameter L is orders of magnitude faster than the ones from the PLD y , as expected. Therefore, to limit the difficulties of solving the differential equations for the time evolution, we assumed that at each timestep the L order parameter is in equilibrium with its instantaneous energy potential. This is equivalent to the limit of the mass m_L in Eq. ?? going to zero. We then took 14 representative experiments, which can be thought of as horizontal slices from Fig. ??(a), solved the differential equations for each of them, and fitted the model parameters to achieve the best total fit.

The results of this fitting procedure is shown in Fig. ??, which shows that the fit is excellent. To get a deeper understanding of the underlying effect, we can look at the evolution of the free energy surfaces for both order parameters, as shown in Fig. ???. The characteristic double well potential for $L \neq 0$ equilibrium is clearly visible, and as expected, when the pulses hit and T_L increases in the term $\alpha(T_L - T_c)L^2$ of Eq. ??, we see that the potential flattens causing the minimum of L to very quickly change, as discussed above. This in turn causes the single-well potential of y to shift as quickly. The dynamics of y is orders of magnitude slower than that of L and due to this instant shift of the energy surface, it will cause an oscillation of y . While the temperature T_L decreases again, L and the minimum of the y potential shift back towards the original equilibrium position. The oscillation of y remains for a relatively long time while this shift is occurring since the damping is not that big (of the order of 4ps). It then becomes clear that if the second pulse can repeat this mechanism while the oscillation of y is still there, it can be increased or decreased depending on the timing. Having this understanding, it becomes clear what the most efficient way is to excite this PLD oscillation. First of all, when the system is relatively close to the phase transition of L , a small increase of temperature causes a large

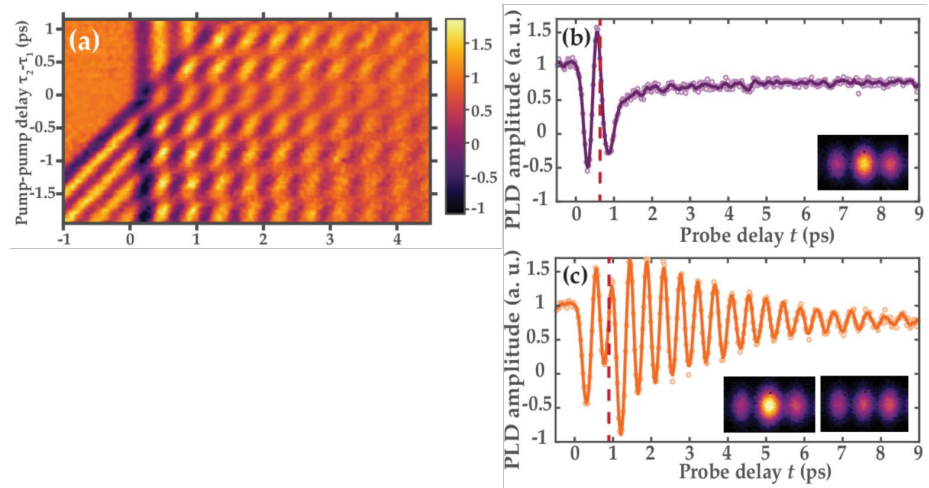


Figure 4.1: Experimental measurements. (a) Heatmap showing different pump-pump delay experiments. Notice the low intensity horizontal band around 0 ps pump-pump delay, where the oscillation amplitude is not at the maximum due to only one big pulse exciting the material and heating it through the phase transition, thus wasting a portion of the energy. The horizontal bands with alternating maximum and minimum magnitudes highlight constructive and destructive interference. (b-c), Magnitude of the strain wave in two extreme control cases, where (b) showcases maximum destructive interference, and (c) close to maximum constructive interference. Solid lines are experimental data (empty circles in figure) smoothed by a Savitzky-Golay filter. b – pump-pump delay of 620 fs, c – pump-pump delay of 845 fs.

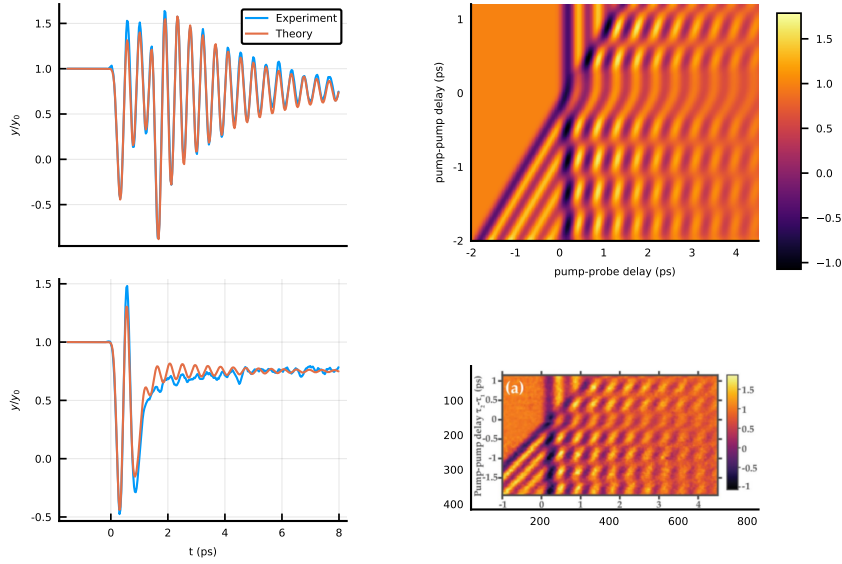


Figure 4.2: Comparison of theoretical fit vs Experiment. (a-b) Two examples of fits to constructive (a) and destructive (b) experiments. (c-d) Comparison of the theoretically generated heatmap (c) with the experimental heatmap (d).

change in the value of L and thus in the shift of the potential for y . On the other hand increasing the temperature of the system above the PT leads to no additional "momentum" being given to y and is thus a waste. Secondly, if the goal is to excite y to the maximum value, the time for damping needs to be as limited as possible. This leads to the case that to gain maximum oscillation magnitude, exciting once every period of y with as much energy to never heat above the PT. This last consideration also depends on the cooling rate of the SDW.

Having fit the model, we can go one step further and try to fit the PLD oscillation to an arbitrary signal shape. To this end we use the fitted model, and predict the timing of a fixed fluence pulse train that will result in the required shape. The results are shown in Fig. ???. This showcases that with an arbitrary pulse train we can achieve indirect, but optimal control of the PLD order parameter.

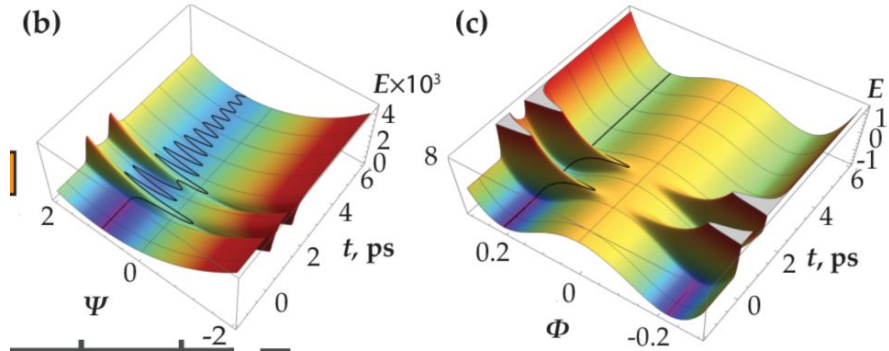


Figure 4.3: Comparison of theoretical fit vs Experiment. (a-b) Two examples of fits to constructive (a) and destructive (b) experiments. (c-d) Comparison of the theoretically generated heatmap (c) with the experimental heatmap (d).

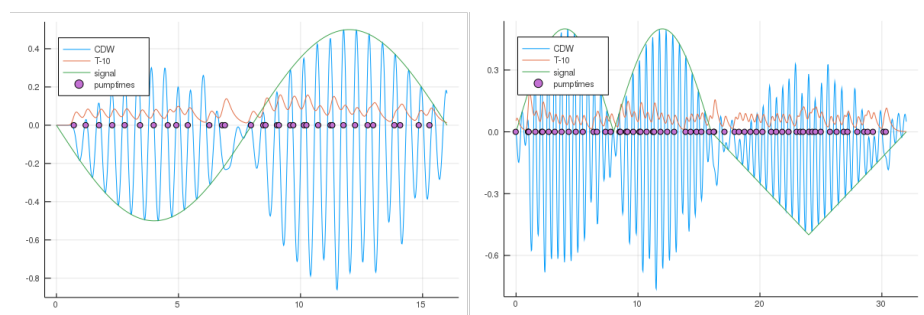


Figure 4.4: Two examples of optimal control. (a) Shows a reproduction of a sinusoidal envelope function, (b) shows the result for more complicated envelope, with an the absolute value of a sinusoidal followed by a half a period of a sawtooth function. The pulse train is highlighted by the purple dots, and the evolution of the temperature of the SDW is given by the orange plot.

Chapter 5

Topological Multiferroic switching; coupling between Magnetism and Ferroelectricity in GdMn_2O_5

5.1 Introduction

Multiferroic materials, where there are multiple ordered structures, have been studied intensely in recent times. The first reason for this is that these orders are usually coupled to some degree, allowing the indirect manipulation of one order by an external perturbation applied to the other. Secondly, this coupling enables a wealth of physical processes to be observed in these materials. Especially materials with relatively low symmetry are a veritable playground to study different effects. In the case under present scrutiny, GdMn_2O_5 , the magnetic configuration that is present in the system breaks inversion symmetry and leads to a small ferroelectric polarization to show up. With an externally applied magnetic field, we can influence the magnetic order and in turn change the ferroelectric polarization through magnetostriction. Experiments have previously shown exactly this effect, but what was previously missed, is that depending on the angle of the applied magnetic field there are three distinguishable switching regimes. As will be discussed later two of these three regimes can be regarded as two topologically trivial extremes, whereas the third one that lives in the crossover region between these two orders can be regarded as topologically non-trivial in the same sense as a Thouless pump.

5.2 GdMn_2O_5

Before describing the underlying theory to describe the processes that happen in GdMn_2O_5 , we focus for a moment on the magnetic unit cell shown in Fig. ??.

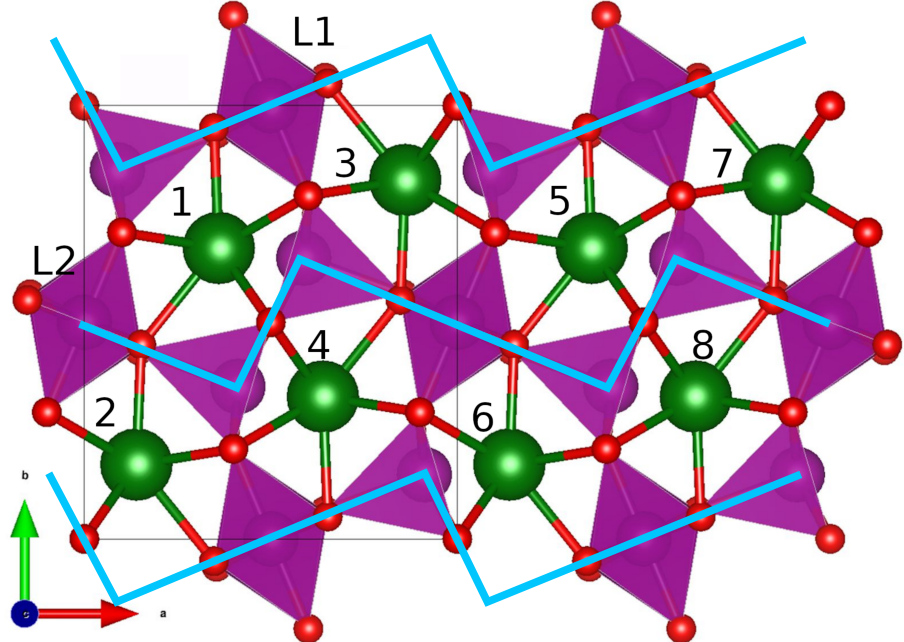


Figure 5.1:

There are two differently oriented chains of Manganese atoms, distinguished by the light blue lines and polygons. Inside these chains there are both tetrahedrally coordinated (Mn^{3+}) and octahedrally coordinated (Mn^{4+}) manganese atoms. Due to the Goodenough-Kanamori rules[citation!] these chains are strongly coupled AFM, leading us to assign one AFM order parameter for each (L_1 and L_2), this amounts to taking the rigid spin approximation in each chain. However, due to the same rules, the chains also couple AFM between each other. When considering the Mn pentagons formed by the two chains around each of the Gd atoms, it becomes clear that there is a magnetic frustration in the system. This will cause the chains to cant a little to be more perpendicular to each other which can then lead to an energy gain through small canting. This frustration breaks inversion symmetry and leads to the first contribution to the ferroelectric polarization through magnetostriction. However, due to the spins of the Gd atoms, and their strong AFM coupling to the surrounding Mn atoms, there is a second contribution to the ferroelectricity. This happens because the Gd atom will move towards the closest tetrahedrally coordinated Mn atom in an effort to optimize the super-exchange energy gain with it. These two contributions add up to a polarization of around $3600 \mu C/cm^2$, which is tiny compared to proper ferroelectrics, but enormous for multiferroics. Lastly due to the size of the spin from the half-filled f-shell Gd atoms (nominally $S = \frac{7}{2}$), dipolar effects may play a role, and each of the Gd spins inside the unit cell need to be considered separately.

5.3 Theory

In light of the above considerations we use a model with two antiferromagnetic order parameters signifying the two orientations of Mn chains, and eight classical spins that describe the different Gd atoms. The Hamiltonian then takes the form:

$$H = \Gamma(\mathbf{L}_1 \cdot \mathbf{L}_2)^2 - \sum_{\alpha} \chi^{-1}((\mathbf{H} \cdot \mathbf{L}_{\alpha})^2 - H^2) \quad (5.1)$$

$$- K_L \sum_{\alpha} (\mathbf{L}_{\alpha} \cdot \mathbf{n}_{\alpha})^2 \quad (5.2)$$

$$+ \frac{1}{2}(g\mu_B)^2 \sum_{i \neq j} \left(\frac{\mathbf{S}_i \cdot \mathbf{S}_j}{r_{ij}^3} - 3 \frac{(\mathbf{S}_i \cdot \mathbf{r}_{ij})(\mathbf{S}_j \cdot \mathbf{r}_{ij})}{r_{ij}^5} \right) \quad (5.3)$$

$$- \sum_i (K_S(\mathbf{N}_i \cdot \mathbf{S}_i)^2 + g\mu_B \mathbf{H} \cdot \mathbf{S}_i) + \sum_{i,\alpha} V_{i\alpha} \mathbf{S}_i \cdot \mathbf{L}_{\alpha}, \quad (5.4)$$

where the first term originates from the competition of the interchain exchange J_{\perp} and the intrachain AFM exchange J_{\parallel} [1], with $\Gamma \sim \frac{J_{\perp}^2}{J_{\parallel}} > 0$ determined by the energy gain on the spin canting, possible when L_1 and L_2 are not collinear. The term with χ represents the gained Zeeman energy when the Mn spins are slightly canted from the purely AFM order inside the chains; terms with K_L and K_S refer to easy-axis anisotropy constants of Mn and Gd spins, respectively. Anisotropy axes for L_1 , L_2 are unit vectors chosen to be aligned with the threefold axes of the tetrahedrally coordinated Mn atoms, i.e. $n_{\alpha} = \pm 23.4^\circ$ respectively. The anisotropy axes for the Gd atoms, N_i , are also unit vectors that alternate as $\pm 12^\circ$. The third line describes the dipole-dipole interactions between Gd ions, which were restricted to five nearest neighbors. It was checked that including further neighbors up to 8.5 Å away didn't lead to qualitative changes of the results. The Heisenberg exchange constants $V_{i,\alpha}$ describe Mn-Gd interactions, where $V_{i,\alpha} = v_1$ for the exchange constant between the Gd and the nearest (tetragonally coordinated) Mn atom and its chain, and v_2 the exchange with the other Mn chain. The model parameters used here are $J_{\perp} = 1.89$ meV, $J_{\parallel} = 26.67$ meV, $K_L = 5.27$ meV, $K_S = 0.2$ meV, $v_1 = 3.33$ meV, $v_2 = 0.15$ meV. The electric polarization P_b , induced by the Heisenberg exchange striction, is given by

$$\begin{aligned} P_b = & \alpha(\vec{L}_1 \cdot \vec{L}_2) + \\ & (\vec{S}_1 - \vec{S}_5)(\beta \vec{L}_2 + \gamma \vec{L}_1) + \\ & (\vec{S}_2 - \vec{S}_6)(\beta \vec{L}_1 + \gamma \vec{L}_2) + \\ & (\vec{S}_3 - \vec{S}_7)(\beta \vec{L}_2 - \gamma \vec{L}_1) + \\ & (\vec{S}_4 - \vec{S}_8)(\beta \vec{L}_1 - \gamma \vec{L}_2), \end{aligned} \quad (5.5)$$

with the model parameters used to fit the experimental data, $\alpha = 0.06 \mu\text{C}/\text{cm}^2$, $\beta = 0.04 \mu\text{C}/\text{cm}^2$, $\gamma = 0.06 \mu\text{C}/\text{cm}^2$. The results are shown in Fig. ??

We proceed by identifying the 2 low and 2 high P_b states in Fig. ??(b) as 1,3 and 2,4 respectively. The magnetic configuration of these states is displayed in panel (h) of the same figure. We then perform a nudged elastic band calculation between these states at different magnetic field strengths while remaining in the

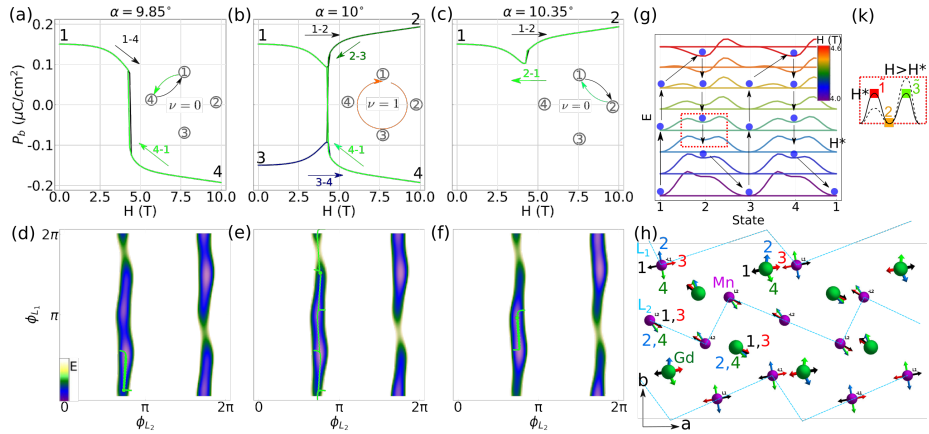


Figure 5.2: (a-c) Evolution of electric polarization P_b during the magnetic field sweep cycle for various magnetic field orientations. The four states are marked by the numbers, and the switching paths indicated by insets and arrows next to the graphs. The colors are used to indicate sequential sweep branches. ν signifies the winding number of each switching regime. (d-f) Trajectories (in yellow) of the AFM order parameter orientations (ϕ_{L_1}, ϕ_{L_2}) through the field sweep cycles in different regimes. The color map shows the energy landscape at an intermediate field inside the hysteresis region. (g) NEB showing the evolution of transition barriers between states 1,2,3,4 as the magnetic field aligned with the magic angle is swept through the hysteresis region. The plots are shifted vertically for clarity. The curve colors encode the corresponding magnetic field strength. The trajectory of the energy minimum due to field sweeps is shown with blue balls and arrows. Coordinated changes of the state energies and barrier asymmetry with magnetic field enable the topological behavior. (h) Spin configurations of the four states, labeled 1...4 in (a). (k) Schematic evolution of the barriers connecting the state 2 to states 1 and 3 away from H^* . Saddle point states are denoted by $\tilde{1}$ and $\tilde{3}$.

4-state hysteresis region, resulting in the evolution of barriers between these states as shown in panel (g), where the color coding is used to denote the magnetic field strength, and the energy graphs are offset for clarity. The arrows and blue balls denote the evolution during the double magnetic field sweep. As expected, there are two degenerate minima at each value of H , at low field these are located at states 1 and 3, then as the field is ramped up they move to favor states 2 and 4. We see that during the sweep the barriers between the different states evolve asymmetrically. As we start in state 1, when the field is ramped up first the barrier towards state 2 decreases faster than the one towards state 4, causing the system to move from 1 to 2. Then as the magnetic field is lowered, the barrier from 2 to 3 increases slower than from 2 to 1. When ultimately state 2 goes from being metastable to a saddle point, the state spills towards state 3, and so on. In order to try and understand where the asymmetric evolution of the barriers comes from, we look at the particular H -field strength where the barriers between state 2 and 1, and 2 and 3 are the same height. This is highlighted by the red dashed box around the blue graph. The inset of panel (k) provides a zoom on this situation. The states on top of the barriers are denoted

by a tilde over the state towards the barrier is oriented, i.e. $\tilde{1}$ signifies the state on the top of the barrier from state 2 towards state 1. We then perform a Taylor expansion in terms of H , around H^* :

$$F(H) = F(H^*) + \frac{\partial F}{\partial H} \Big|_{H=H^*} (H - H^*) + \dots, \quad (5.6)$$

for each of the states and subtract the result. Using $\frac{\partial F}{\partial H} = M$ we find

$$F_{\tilde{1}}(H) - F_{\tilde{2}} = (M_{\tilde{1}} - M_{\tilde{2}})(H - H^*). \quad (5.7)$$

[show how to calculate M?] This means that to first order the evolution of the barrier asymmetry is given by the difference magnetization of the states on top of the barriers. Indeed we find that the magnetizations are different from our simulations, confirming that this is at least a part of the reason for the asymmetric evolution of the barriers. Moreover, due to the symmetry of the system, this asymmetry is opposite when the field is swept up, as compared with when the field is swept down. This causes the unidirectional movements through the four states.

5.4 Simplified Model

Having found a description for the situation in the complicated material GdMn₂O₅ using the model ??, one may wonder what the minimal requirements are to have a similar four-state behavior where the spins rotate 360° while the applied field only oscillates along a single axis. We look to the spin configurations of Fig. ??(h) for inspiration. It is clear that, although necessary for the P_b behavior, it seems that the chain with Mn moments most parallel to the applied field does the full rotation, while the other chain merely oscillates around its starting position. The Gd moments seem to follow the behavior of the chain they are most strongly coupled to. This warrants an attempt to explain the observed behavior using only a single chain with its Gd moments. In the particular case where the magic angle is along $\alpha = +10^\circ$, we keep L_1, S_2, S_3, S_6 and S_7 as the variables in the model. We also assume that the easy axis of Gd is not that important. This leaves us with the following Hamiltonian, which we will split up in two parts, one with the dipolar terms H_{dip} and one with all the other terms H' :

$$H = H' + H_{dip} \quad (5.8)$$

$$H' = J_1(\mathbf{S}_2 + \mathbf{S}_3 - (\mathbf{S}_6 + \mathbf{S}_7)) \cdot \mathbf{L}_1 - g\mu_B(\mathbf{S}_2 + \mathbf{S}_3 + \mathbf{S}_6 + \mathbf{S}_7) \cdot \mathbf{H} \quad (5.9)$$

$$+ K_L(\mathbf{L} \cdot \mathbf{n}) \quad (5.10)$$

$$H_{dip} = \frac{1}{2}(g\mu_B)^2 \sum_{i \neq j} \left(\frac{\mathbf{S}_i \cdot \mathbf{S}_j}{r_{ij}^3} - 3 \frac{(\mathbf{S}_i \cdot \mathbf{r}_{ij})(\mathbf{S}_j \cdot \mathbf{r}_{ij})}{r_{ij}^5} \right). \quad (5.11)$$

Due to the symmetries of this model and the geometry of the material we end up with two copies of one spin in the first half of the magnetic unit cell and one in the second half of the unit cell, with the chain inbetween (see Fig. ??).

This causes $S_2 = S_3$ and $S_6 = S_7$, and thus allows us to look at a single one of the two copies. Again keep only nearest neighbor dipolar terms, and

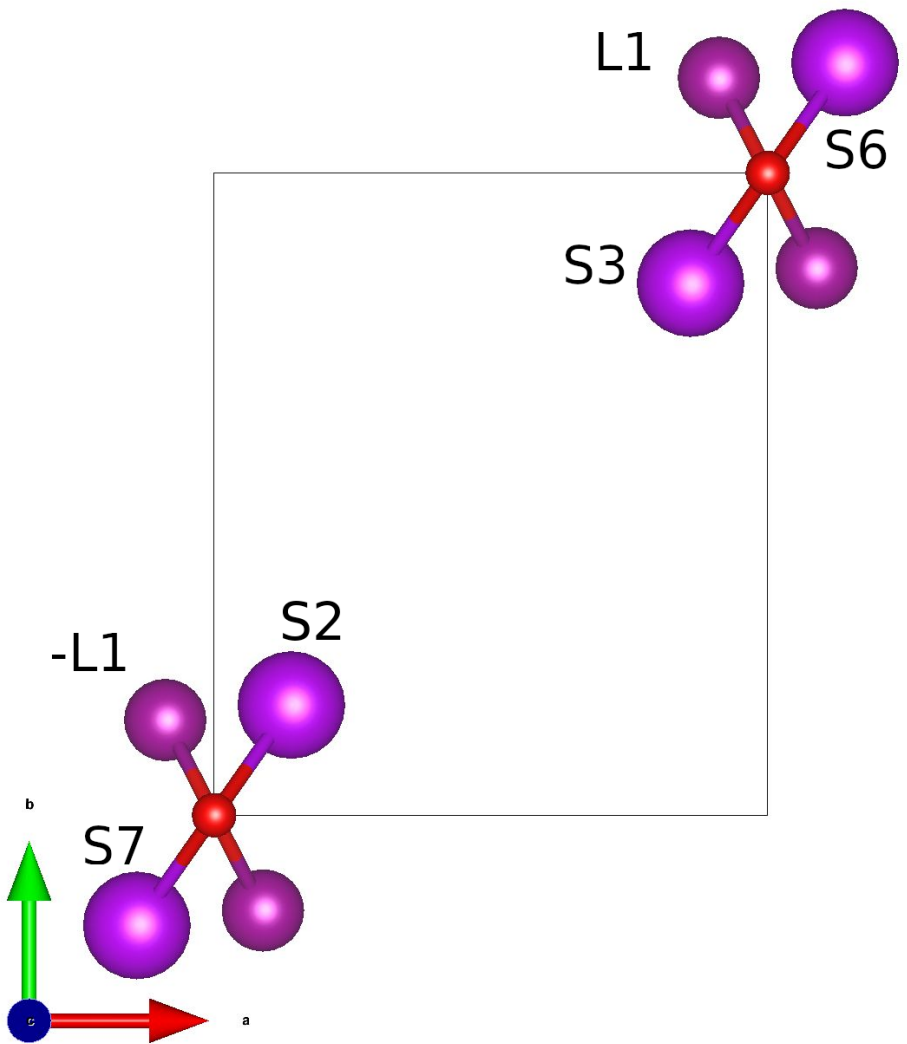


Figure 5.3: Simplified single chain model.

assuming no anisotropy for the Gd spins, we end up with

$$H' = 2J_1(\mathbf{S}_3 - \mathbf{S}_6) \cdot \mathbf{L}_1 - 2g\mu_b(\mathbf{S}_3 + \mathbf{S}_6) \cdot \mathbf{H} \quad (5.12)$$

$$+ K_L(\mathbf{L} \cdot \mathbf{n}) \quad (5.13)$$

$$H_{dip} = (g\mu_B)^2 \left(\frac{\mathbf{S}_3 \cdot \mathbf{S}_6}{r_{36}^3} - 3 \frac{(\mathbf{S}_3 \cdot \mathbf{r}_{36})(\mathbf{S}_6 \cdot \mathbf{r}_{36})}{r_{36}^5} \right). \quad (5.14)$$

Bibliography

- [1] A B Sushkov et al. “Electromagnons in multiferroic RMn₂O₅compounds and their microscopic origin”. In: *Journal of Physics: Condensed Matter* 20.43 (Oct. 2008), p. 434210. DOI: 10.1088/0953-8984/20/43/434210.